# Inflation and Asymmetric Collapse at Kilauea Summit during the 2018 Eruption from Seismic and Infrasound Analyses

**Voon Hui Lai[1,2], Zhongwen Zhan[1], Osamu Sandanbata[3], Quentin Brissaud[1,4] and Meghan S. Miller[2]**

[1]Seismological Laboratory, California Institute of Technology, USA.

[2]Research School of Earth Sciences, The Australian National University, Australia.

[3]National Research Institute for Earth Science and Disaster Resilience, Japan.

[4]Norwegian Seismic Array (NORSAR), Norway.

Corresponding author: Voon Hui Lai (voonhui.lai@anu.edu.au)

**Key Points:**

- We characterized the large seismic events at the Kilauea summit using particle motion, infrasound, and seismic moment tensor inversion.
- Near-field seismic observation is essential to resolve the isotropic contribution due to inflation of the Halema'uma'u reservoir.
- Two independent moment tensor inversions show that the caldera collapsed asymmetrically along the northwest corner.

**Abstract**

Characterizing the large M4.7+ seismic events during the 2018 Kilauea eruption is important to understand the complex subsurface deformations at the Kilauea summit. The first 12 events (May 17 - May 26) are associated with the explosive eruptions and the remaining 50 events (May 29 - August 02) are accompanied by large-scale caldera collapses. Resolving the source location and mechanism is challenging because of the shallow source depth, significant non double-couple components, and complex velocity structure. We showed combining multiple geophysical data from broadband seismometers, accelerometers and infrasound is essential to resolve different aspects of the seismic source. The seismic moment tensor solutions using near-field summit stations show the early events are highly isotropic. Infrasound data and particle motion analysis identify the inflation source as the Halema'uma'u reservoir. For the later collapse events, two independent moment tensor inversions using local and global stations consistently show that asymmetric slips occur on inward-dipping normal faults along the northwest corner of the caldera. While the source mechanism from May 29 onwards is not fully resolvable seismically using far-field stations, infrasound records and simulations suggest there may be inflation during the collapse. The summit events are characterized by both inflation and asymmetric slip, which are consistent with geodetic data. Based on the location of the slip and microseismicity, the caldera may have failed in a 'see-saw' manner: small continuous slips in the form of microseismicity on the southeast corner of the caldera, compensated by large slips on the northwest during the large collapse events.


## Plain Language Summary

Characterizing the large seismic events that occurred at the Kilauea summit is important to understand the subsurface deformation process during the 2018 eruption. There are a total of 62 events where the first 12 events are accompanied with plume emission and the later 50 events are associated with large collapses within the caldera. There are several challenges in characterizing these events due to the complex volcanic environment but can be overcome by using multiple geophysical datasets including seismic waves that travel in the Earth and infrasound that travels in the atmosphere to provide a more complete perspective on the seismic source – its location and how it deforms. While the shallow magma reservoir at the summit experiences an overall deflation throughout the eruption, we found that the reservoir inflates temporarily during the earlier seismic events. For the later collapse events, the caldera slipped on only one side instead of a complete subsidence of the entire caldera which is commonly assumed. Our finding of both inflation and one-sided slip is consistent with other independent studies and suggests this asymmetric slip may be a common feature for basaltic volcanoes like Kilauea.

## 1 Introduction

The 2018 Kilauea eruption completely transformed the Kilauea summit from its previous state of small-scale continuous eruptions, starting from the drainage of the lava lake at the vent within the Halemaʻumaʻu crater to the eventual large-scale caldera collapse (Neal et al. 2019). During the 2018 eruption, 62 large seismic events were recorded at the Kilauea summit: the initial 12 events from May 17 to May 26 had moment magnitudes (Mw) between 4.3 and 4.7, and were often accompanied by ash plume explosions; the remaining 50 events from May 29 to August 2 were stronger (average Mw 5.3) and associated with broad scale collapses (Neal et al., 2019). These seismic events were potentially related to the dynamic, transient process at the subsurface reservoir. The presence of a shallow reservoir was well-established through modeling the eruption behavior at the summit prior to 2018 including the fluctuations of the lava lake level, several Very-Long-Period (VLP) seismic events, and deflation-inflation episodes. Analyses based on these observations including tilt inversion (Anderson et al., 2015), geodetic modeling using interferometric synthetic aperture radar (InSAR) data (Baker and Amelung, 2012), seismic modeling of the VLP events (Dawson et al., 2010, Chouet et al., 2010), and modeling of the lava-lake sloshing mode during the VLP events (Liang et al., 2020) pointed to a reservoir slightly east of the Halemaʻumaʻu crater at a depth of between 1 - 2 km below the surface. The reservoir, namely Halemaʻumaʻu, is thought to be hydraulically connected to the vent and the lava lake (Patrick et al., 2015), a deeper magma reservoir (Poland et al., 2014) and to the rift zone downstream (Anderson et al., 2015; Patrick et al., 2019).

Characterizing the seismic events in the 2018 eruption can help us to infer the deformation process beneath the summit and its relation to the overall eruption sequence. However, describing complex seismic source processes at volcanic regions is challenging due to observational limitations. Many caldera collapses at remote locations are monitored by seismic stations at teleseismic distances as in-situ stations are rare. As a result, seismic source studies are restricted to only using long-period surface wave data recorded in the far-field which have several disadvantages. First, long-period waves have little sensitivity to the focal depth for shallow sources. Given magma reservoirs can occupy a wide range of depths (1- 20 km), accurate determination of source depths can help pinpoint the deforming reservoir. Furthermore, due to zero traction at free surface, the long-period seismic waveforms related to dip-slip components are weakly excited for shallow seismic sources (Julian et al., 1998). Caldera collapse often generates shallow seismic sources with significant non double-couple contributions, i.e. isotropic and vertical compensated-linear-vector-dipole (CLVD), which are highly correlated (Kawakatsu, 1996). The correlated waveforms make it hard to distinguish source processes such as reservoir pressurization, crack opening or closing, or shear slip around a ring fault (Fukao et al., 2018; Sandanbata et al., 2021). The combined issues of indeterminate focal depth and weak excitation for shallow source can be overcome using higher frequency waves up to 0.15 Hz; However, the trade−off issue between isotropic component and vertical CLVD still remains (Hejrani and Tkalčić, 2020). Characterization of non double-couple sources can be improved by increasing the coverage of the source focal sphere. An example is the analysis of the volcanic earthquake at the submarine Smith Caldera near the Izu-Bonin Arc in the western Pacific. The pressure gauge array which samples the upper hemisphere of the source radiation pattern, recorded a strong tsunami motion, meaning the caldera seafloor is uplifted and this process could not be uniquely determined from seismic data alone (Fukao et al, 2018).

The 2018 Kilauea summit eruption were recorded by several types of geophysical instruments at the summit and southern part of the island including broadband seismometers, accelerometers, and infrasound arrays (Figure 1), providing a unique opportunity to characterize the seismic sources and infer the underlying deformation process. In this study, we employed multiple techniques including particle motion analysis, seismic moment tensor inversion, infrasound travel time study, and infrasound simulations. In the moment-tensor inversion, near-field summit stations are essential to resolve the isotropic contribution. Using regional data of relatively high frequency waves also allows for stable inversions of the faulting mechanism. Infrasound and particle motion analyses further provide the crucial constraints on source depth and location which is hard to resolve from seismic source inversions alone. Finally, we confirmed our results with an independent teleseismic moment tensor inversion, compared our results to geodetic analysis, and described the chronology of the Kilauea summit deformation.

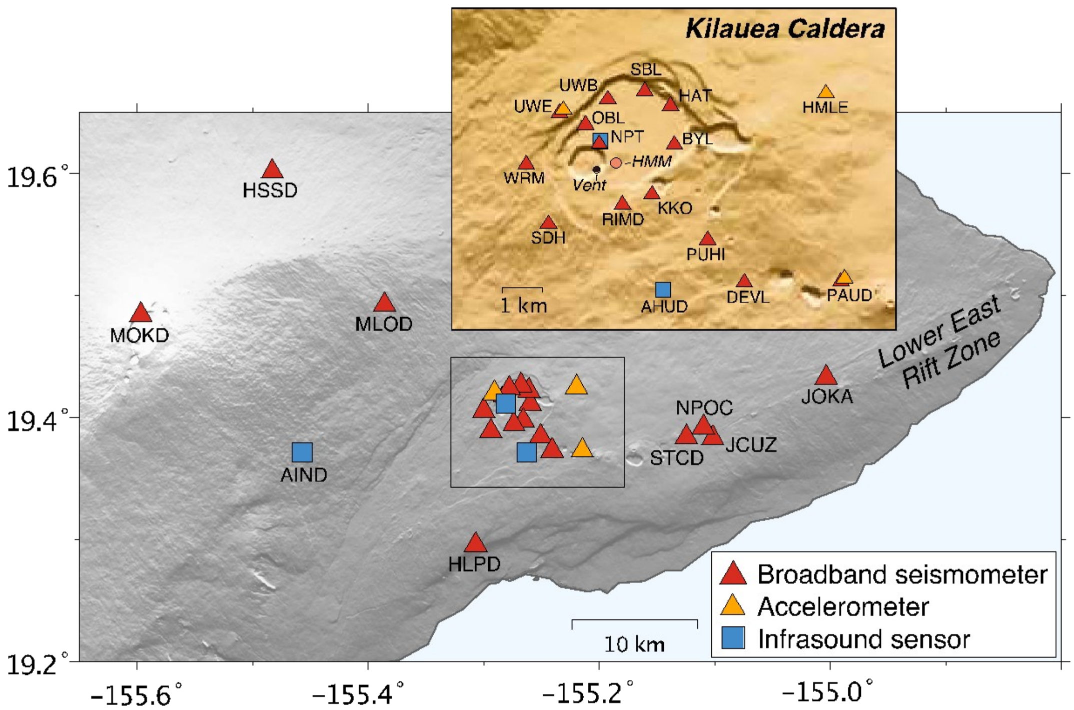


**Figure 1**. Map of Kilauea Caldera and Lower East Rift Zone before the 2018 eruption. The inset focuses on the summit including the smaller Halema‘uma‘u crater (dashed line), the vent with an active lava lake (black dot) and the predicted centroid location of the Halema‘uma‘u (HMM) magma reservoir (orange circle). The map also shows the regional geophysical instruments maintained by USGS Hawai’i Volcano Observatory (HVO): broadband seismometers in red triangles, accelerometers in yellow triangles, and infrasound sensors in blue squares.

## 2 Event location from particle motion analysis

Particle motion provides an independent constraint to locate the source and track how seismic source migrates, which is challenging in seismic moment tensor inversions due to reduced sensitivity to location at long periods. Previous work by Kawakatsu et al. (2000) found that the summit stations recorded the near field static displacements of the large seismic events, which showed a rectilinear polarization pointing towards the source location. To measure the particle motions, we applied a long period filter (20 – 50 seconds) to the seismic waveforms and measured the back-azimuth by treating the two horizontal components as a covariance matrix and calculating the angle of rotation of the eigenvector with the largest eigenvalue. Strong velocity heterogeneities and sharp topographic change can distort the ray path from the direct great-circle path, causing the particle motions to not project onto a common point. Liang and Dunham (2020) have shown that the seismic signals from the past VLP events shortly before the first large explosive events originate from the known Halemaʻumaʻu (HMM) reservoir. Therefore, we compare the particle motion of individual stations measured from the seismic events during the eruption and these VLP events to identify if the source is the same. We found that the horizontal particle motions for the first 12 events (May 17 to May 26) overlap greatly with the particle motions from the past VLP events, indicating an identical seismic source localized at the HMM reservoir (Figure 2). The analysis using the radial and vertical particle motions also showed minimal difference in the dip angle (Figure S1), meaning the events have a common source depth, determined to be at 1 km by Liang and Dunham (2020).

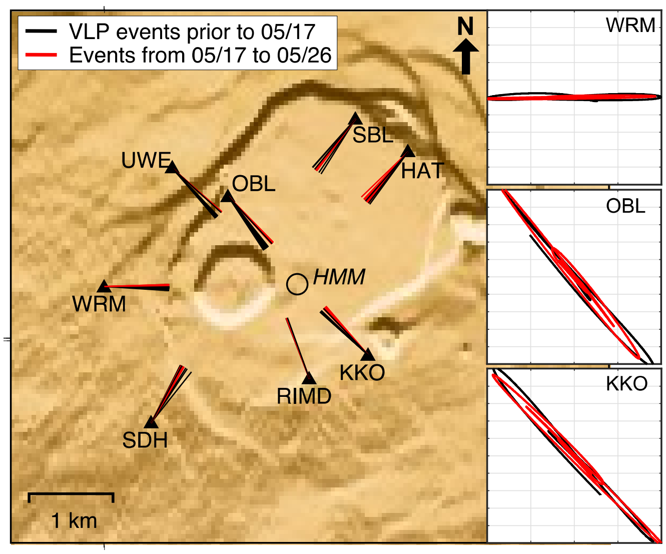


**Figure 2**. Back azimuths of horizontal particle motions recorded by broadband seismometers on the summit for the Very Long Period (VLP) events prior to May 17 (i.e., March 15, April 6, May 9 and events studied by Liang et al. (2019) between May 3 and May 7) and the first twelve explosive seismic events (May 17 to May 26 in red). Right plots show the comparison of particle motions from a VLP event to an explosive event recorded at station WRM, OBL and KKO.

We further analyzed the horizontal particle motion of the accelerometer recordings (UWE, HMLE, and PAUD) which remained unclipped throughout the eruption. The particle motion showed four distinct episodes (Figure 3). For the first 12 events, the accelerometer closest to the caldera, UWE, showed a consistent back-azimuth, indicating a localized source. For the remaining 50 events, we see a small (less than 5 degree) but systematic change in back-azimuth at station UWE and PAUD with a marked transition around June 7-8 and June 24-25. The decrease in back-azimuth for UWE which is located northwest of the caldera, and the increase in back-azimuth for PAUD, which is at the south of the caldera, suggest that the seismic source is migrating eastward. Given HMLE is located to the east of caldera, we expect minimal changes in the back-azimuth from an eastward migration of the source. The timing of the transition determined by the particle motion corroborates with the changes in displacement behavior observed by several global position system (GPS) stations at the caldera (Tepp et al., 2020).

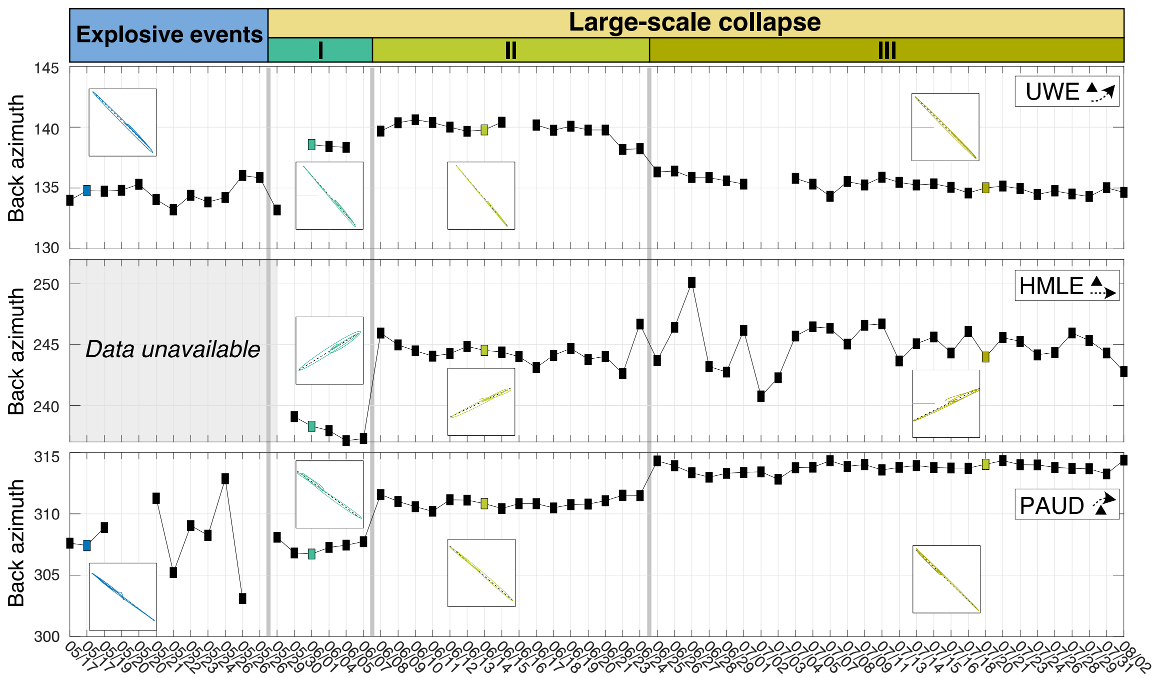


**Figure 3**. Back azimuths of horizontal particle motions recorded at three accelerometers (UWE, HMLE and PAUD) for all large seismic events from May 17 to August 2. A selection of particle motions for some events, which are color-coded, are plotted and the measured back azimuths are marked in thick dashed line. Unreliable measurements are discarded. The arrows in the top right insets show the direction of the source migration with respect to the station location.

## 3 Moment tensor analysis using summit and regional stations

### 3.1 Methodology

Seismic-source tensors provide important information about the deformation process including event size, pressurization, and fault geometry. By decomposing the source tensor (e.g., Chapman and Leaney, 2012), we can determine the relative contribution of the isotropic term, which is volumetric and represents pressure change, and the deviatoric term which describes the displacement discontinuity on a fault and can be further decomposed into double-couple (DC) and CLVD components. In this study, we used the generalized Cut-and-Paste (gCAP) moment-tensor inversion method (Zhao and Helmberger, 1994; Zhu and Helmberger, 1996; Zhu and Ben-Zion, 2013) which allows independent time shifts for all three components while cross-correlating the predicted and observed waveforms to minimize the errors due to inaccurate event location and velocity model. The time-shift window is carefully selected to avoid cycle-skipping.

The Green's functions are computed with the frequency-wavenumber method described in Zhu and Rivera (2002) using a 1-D velocity model constructed from a layer average of the 3-D local P-wave seismic tomography (Lin et al., 2014). We approximate the source time function with an isosceles triangle and determine the duration through grid search between 1 and 25 seconds.

We used a selection of broadband seismometers maintained by the USGS Hawaiian Volcano Observatory, 14 near-field stations within 3 km radius from the summit and 8 regional stations within 35 km radius (Figure 1). The near-field summit stations, which are directly above the source and sensitive to the upper hemisphere of the source radiation pattern, are crucial to determine the isotropic component of the moment tensor as the isotropic and vertical-CLVD terms produce similar azimuthal radiation patterns in the far-field. To illustrate, the synthetics from the GCMT solution, which has a strong vertical-P CLVD component, and the best deviatoric solution determined by gCAP fit the regional data and not the near-field data recorded at the summit (Figure S2 and S3). Full moment tensor solution that searches for all DC, CLVD and isotropic terms can fit the near-field data well for all azimuths (Figure 4a). However, these near-field data are only available for the initial 12 events and are clipped for the remaining 50 events. Hence, we performed separate inversions for the early (Section 3.2) and later events (Section 3.3).

Stations further away on the island are not used as they do not show clear single elliptical-particle motions owing to a strong multipathing behavior, indicating surface waves arriving at multiple azimuths. Summit stations are limited to the vertical component as the horizontal components at long period are highly susceptible to tilt due to deflation or inflation processes (Wielandt and Forbriger, 1999). Waveforms recorded at near field (< 3 km) are weighted less than the regional data to prevent their large amplitude from dominating the inversion results. Based on the particle-motion results, the source is set at the HMM reservoir (19.4069°, -155.2752°; from Baker and Amelung, 2012), which is similar to centroid location determined by Liang and Dunham (2020). The inversion is repeated for a range of source depths between 0.1 and 5 km.

### 3.2 Early explosive events (05/17 – 05/26)

The full moment tensor inversion results show that for the first 12 events, the best-fit solutions have moment magnitudes between Mw 4.37 to 4.95 with high isotropic contribution (average 72.4%), significant DC (average 27.4%), and negligible CLVD (< 1 %) (Figure 4b). The strike, rake, and dip of the focal mechanisms are also similar throughout the events (average 66/-72/49) and are stable as supported by the bootstrapping analysis (Figure S4). Grid search results show that most of the early events fit well at a depth range between 0.7 and 2.0 km, with the best depth at 900 m from the surface (Figure S5). The depth, with the uncertainty, is similar to the depths estimated for HMM reservoir from seismic studies at ~1 km (Chouet et al., 2010; Liang and Dunham,2020) and from geodetic inversions at ~2 km (Baker and Amelung, 2012; Anderson et al., 2019).

The source durations of these events range between 10 to 20 seconds which are an order of magnitude longer than the durations for similar-magnitude tectonic earthquakes (Kanamori and Brodsky, 2004). The source durations correlate well with the length of the long-period pulse in the raw waveforms (Figure S6) and have no obvious correlation with other parameters such as event magnitude or event time. Events 4 and 5 have exceptionally long source durations exceeding the period bandwidth of the input waveforms hence their moment tensor solutions are unreliable. The use of time shifts in the gCAP inversion prevents us from determining the centroid time of the events.

**Figure 4**. **(a)** Plot of the best-fitting full moment tensor solution inverted for explosive event 2, which is highly isotropic (74%) with the strike, dip and rake value of 232, 41 and -103 respectively. The waveforms are surface wave displacement filtered at 0.03 – 0.08 Hz. The observed displacements are plotted in black and the synthetics in red. The distances measured in kilometers and azimuth of the stations to the epicenter, and the time shifts used in gCAP, correlation coefficient (cc) and waveform misfit are also listed. **(b)** Graph shows the similarity of the best-fitting full moment tensor solutions, focal mechanisms, and the contributions of the isotropic, CLVD, and double-couple components for the 12 explosive events between May 17 and May 26. The moment tensor solutions for events 4 and 5 (May 20a and May 20b), marked with asterisks, are poorly determined due to the anomalously long source duration.

### 3.3 Late collapse events (05/29 – 08/02)

For the later events, the isotropic contribution cannot be determined due to the fits of deviatoric and full moment tensor solutions to the waveforms are similarly good (Figure 5a). Hence, we focused on the deviatoric solution to resolve the fault geometry (strike, rake, dip) and the strength of CLVD term. The input waveforms are filtered between 12.5 to 50 seconds (0.02-0.08 Hz). The hypocenter is fixed at the HMM reservoir location as the regional waveforms are insensitive to the small changes in location around the caldera. The source depth is fixed at 450 m, informed by infrasound simulations (details in Section 4.2). The preferred source duration is 5 seconds based on grid search results.

The inversion results show that the remaining 50 events are shear slips along inward-dipping normal faults with minimal CLVD component (< 5%) (Figure 5b). The events evolve throughout the eruption with three marked transitions in the focal mechanisms. Between May 29 to June 7, the events have a relatively high CLVD term (maximum 20 %) with an average strike/rake/dip of 73/-50/75. From June 8, the strength of CLVD term decreases, along with changes in the strike, rake, and dip to a new average of 69/-38/75 until June 25 when the focal mechanism stabilized and remained fairly constant until the end of the collapse sequence. The later focal mechanisms have a small CLVD component, and an average strike, rake, and dip of 74/-52/75., The transitions coincide with the changes in particle motion determined from accelerometers which show the source migrated eastward over time (Figure 3). The nodal plane is selected to be striking northeast-southwest in order to be consistent with the increasing strike value and the eastward source migration along the caldera. The inversion results suggest the roof block above the caldera has collapsed asymmetrically at its northwest corner, instead of a commonly assumed complete ring-fault slip. There may be a significant isotropic component associated with these events as observed in the rapid inflationary steps in tilt data (Anderson et al., 2019; Segall et al., 2019), but is not resolved for these events.

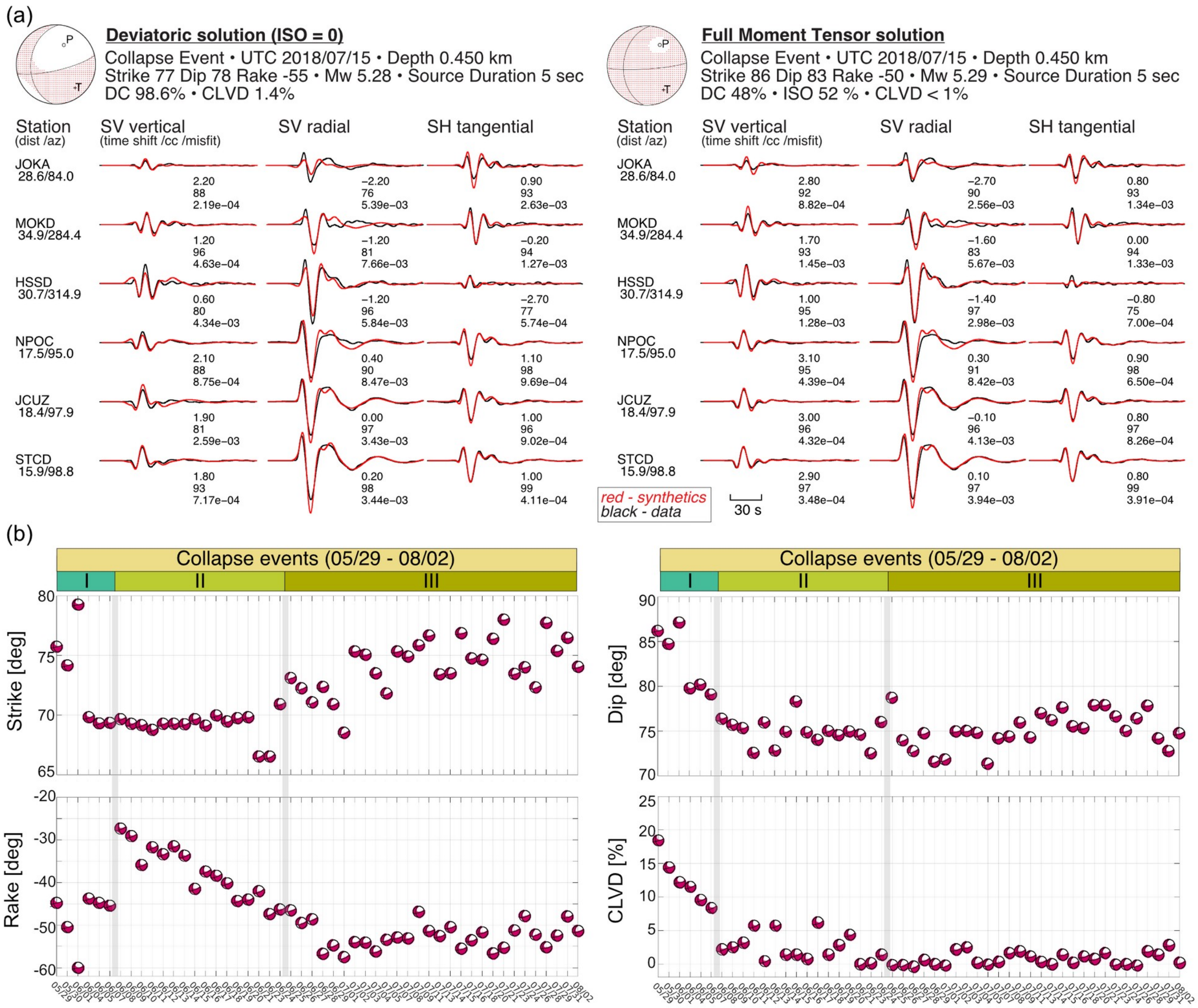

**Figure 5**. **(a)** Figure shows both best fitting deviatoric (left) and full moment tensor (right) solutions for collapse event 51 (July 15, 2018) can fit the regional waveforms well. The observed displacements are plotted in black and the synthetics in red. The distance and azimuth of the stations to the epicenter, and the time shift used in gCAP, correlation coefficient (cc) and waveform misfit are listed. **(b)** Figure shows the best-fitting deviatoric solutions for all 50 collapse events between May 29 to August 2. The changes in strike, rake, dip, and CLVD component follow closely the transitions (marked by grey lines) observed in the particle motion measurements (Figure 3).

## 4 Source depth from infrasound analysis

Infrasound are pressure waves with frequencies below 20 Hz that can be generated during a plume eruption into the atmosphere or by shallow seismic source which its seismic energy couples with the free surface and propagates in the air at acoustic sound velocities (Fee and Matoza, 2013). As infrasound is sensitive to upward radiating energy like the near-field summit stations, it can provide additional constraint on the source processes (e.g., Fukao et al. 2018). During the 2018 eruption, the nearby AHUD infrasound array recorded a variation in infrasound arrival-time and waveform shape (Figure S7). For each event, we can compute the theoretical arrival time based on the sound velocity and the distance from the vent to the sensor. For the first 12 events, AHUD records fairly weak pressure signals, with occasional strong-upward pulses that are significantly delayed from their expected acoustic arrival times. These upward pulses are also observed during the VLP events prior to the large seismic events on March 15, April 6 and May 9, where the summit webcam recorded ash plumes exiting the vent. For the remaining 50 events, there are two distinct arrivals: (1) weak high frequency waves traveling at seismic Rayleigh-wave velocity and (2) a strong low frequency pulse with initial downward polarity traveling at acoustic speed.

### 4.1 Infrasound observations for early events

The arrival time of the compressional peaks are clearly observed by infrasound sensors at multiple distances (< 1 km, 4.5 km and 19 km; Figure 6a). The origin time is assumed to be the catalog origin time for the events during the eruption and the seismic arrival time at the closest seismic station (NPT; < 1 km) for the previous VLP events. The waveforms are plotted at reduced time, which is the total time subtracted by the travel time from the vent to the sensor. On March 15 and April 6, we observed that the strong infrasound peak arrived at about the zero mark which is the expected acoustic arrival time. From May 9 to May 26, the arrival of the infrasound peak is progressively delayed in time. Given the delayed arrival time, we hypothesize that the infrasound pulse observed during the early events are not a direct result from the seismic event but from the degassing process which initiates at the reservoir, propagates upward through a conduit, and exits at the vent creating an upward compressional pulse. The propagation time in the conduit is controlled by the lava lake elevation, which was visible at the vent throughout the spring of 2018 and started draining at an estimated rate of 2.2 meter per hour on May 2 (Anderson et al., 2019). Theoretically, when the conduit was completely filled, the signal arrived at the sensor at a time corresponding to the vent-to-sensor distance. As the lava lake began to drain, the length of drained conduit increased, delaying the infrasound pulse. Towards the end of the first 12 events, the lava level reached the reservoir depth and the entire conduit was drained. This propagation behavior and time delay is similar to that observed at Miyake-jima by Kobayashi et al. (2005) where the signal from the degassing process burst through the lava lake surface layer traveling in the conduit at a distinct velocity before propagating as an infrasound pulse at acoustic speed from the vent to the sensor.

### 4.2 Source depth constrained from infrasound

From the infrasound arrival-time measurements, we constrain the velocity of the rising plume, the speed of degassing signal in the lava medium and most importantly the length of the conduit. The relation between the arrival time of the infrasound pulse and the propagation distance is described as total time, $t_{total} = (1/V_c)d + (1/V_l)(h - d) + (1/V_a)x$, where $h$ is the length of conduit, $d$ is the length of the drained conduit, $x$ is the distance from the vent to the sensor, $V_c$ is the velocity of the rising plume, $V_l$ is the speed of degassing signal in the lava medium, and $V_a$ is the acoustic speed at surface (Figure 6b). The term $(1/V_a)x$ is known. Assuming the draining rate, $R$, remains constant over the course of the eruption, $d$ is calculated by taking $d = R\Delta T$, where $\Delta T$ is the time elapsed between each eruption. To estimate $h$, $V_c$, and $V_l$, an additional condition is needed. Based on the hypothesis, an appropriate condition is that the entire length of the conduit is completely drained by event 12, that is $t_{last} = (1/V_c)h$. Event 12 had a very weak infrasound pulse, so we take the clear signal from a slightly earlier event on the same day (Event 10) as an approximation. With this condition and the infrasound time measurements, we obtained the values of $V_c$, $V_l$ and $h$ from a simple linear regression of the total time, $t_{total}$ and time elapsed, $\Delta T$. We estimated $h$ to be 1,280 m, $V_c$ to be 37 m/s, and $V_l$ to be 326 m/s (Figure 6c). The values of $V_c$ is in the same order of magnitude as strong Strombolian-type degassing (31 – 34 m/s in Patrick et al. (2007); 38 – 53 m/s in Taddeucci et al. (2012)) and is comparable to the previously recorded plume velocities at Kilauea (ranging between 5.8 and 16.6 m/s in Fee et al. (2010)). The estimated $h$ is slightly deeper than the depth of the seismic source obtained from the seismic moment tensor inversion at 900 m, but still within the uncertainty from inversion (0.7 to 2 km). The estimated $h$ is also consistent with the lava lake elevation at the end of the explosive events at 1260 m, which is estimated from the draining rate (Figure S8).

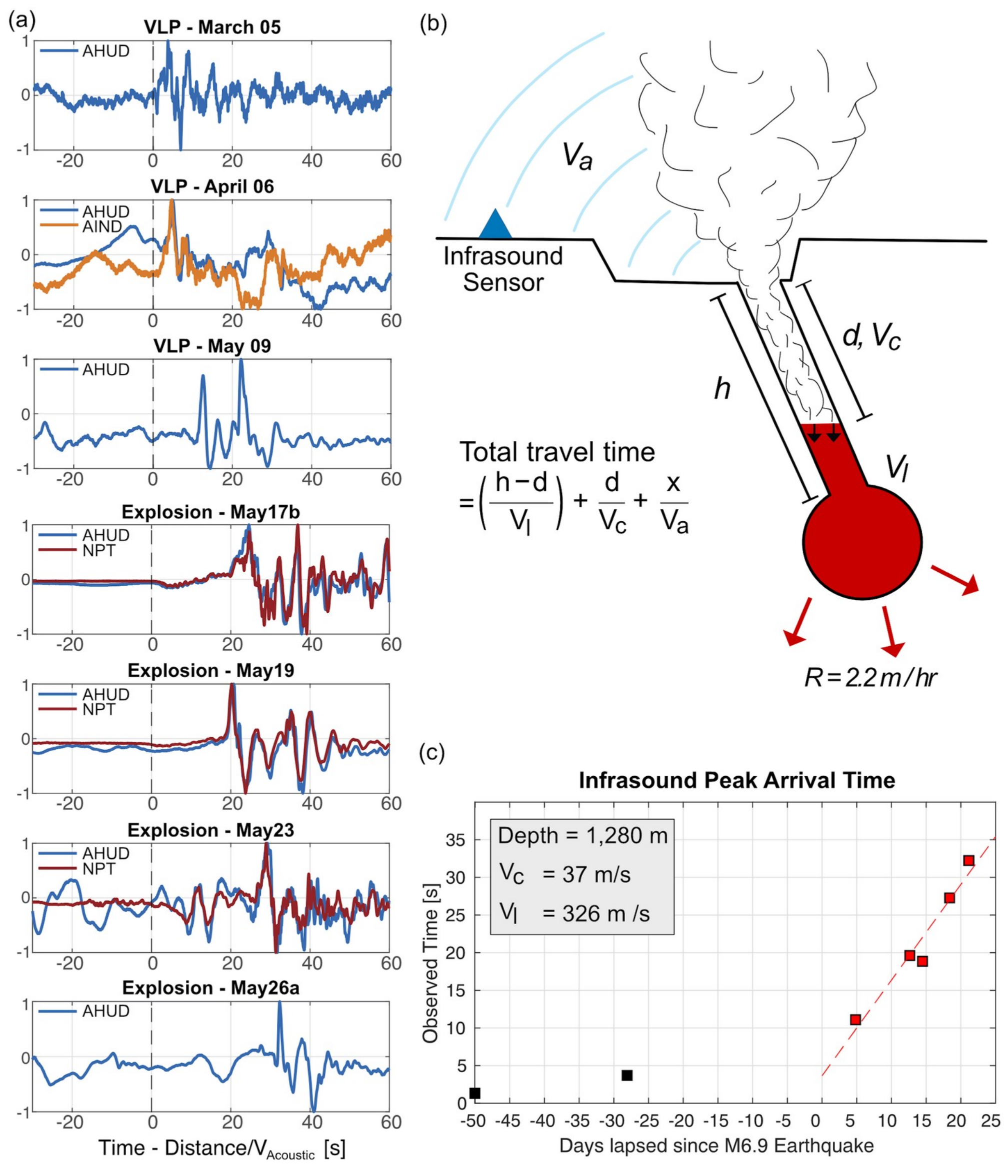

**Figure 6**. **(a)** Plot shows the raw infrasound data for three VLP events and four selected explosive events. The data are plotted in normalized amplitude at reduced velocity, corrected for the travel time from the vent to the sensor. **(b)** Schematic shows the variables involved in calculating h, i.e. length of the conduit, which include: *d,* the length of the drained conduit; *x,* the distance from the vent to the sensor; $V_c$, the velocity of the rising plume; $V_l$, the speed of degassing signal in the lava medium; and $V_a$, the acoustic speed at surface. The lava lake is draining at an estimated speed of *R* (2.2 m/hr from Anderson et al., 2019). **(c)** Graph shows the observed time delay in the peak arrival against the number of days elapsed since the M6.9 earthquake. The events in red are used in the inversion which gives the estimated depth of 1280m, 37 m/s for $V_c$ and 326 m/s for $V_l$.

### 4.3 Infrasound simulation for explosive and collapse events

We also tested the infrasound data against the seismic moment tensor solutions. To simulate, we used a hybrid Galerkin – 2D spectral element method (Brissaud et al., 2017) which accounts for the elastic wave propagating away from the seismic source and the acoustic wave generated due to the coupling between solid Earth and atmosphere. The effects of atmospheric structure and variability can be ignored for short distance simulation (4.5 km). Simulation using the highly isotropic solution from the earlier events generates synthetics which have very weak amplitudes and arrive at the expected acoustic travel times (Figure 7a), supporting the previous hypothesis that the observed late strong upward pulse does not originate from seismic source. For the later collapse events, infrasound simulations using the deviatoric moment tensor solution are able to reproduce the seismic-acoustic coupling of both the early, high frequency Rayleigh pulse and the late, low frequency, high amplitude acoustic pulse (Figure 7b).

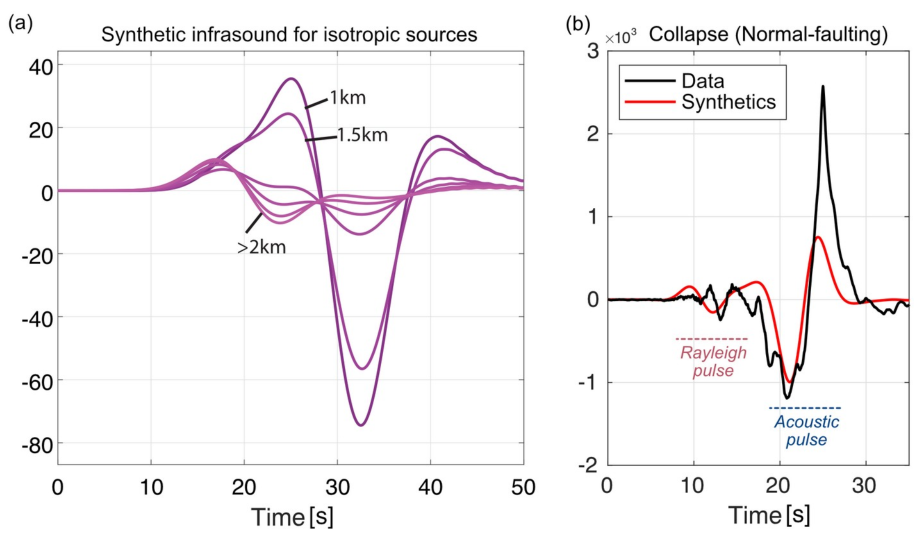


**Figure 7. (a)** Plot shows the comparison of synthetic infrasound generated at different source depths using the highly isotropic solution from event 2. **(b)** Plot shows the comparison of observed infrasound (black) with synthetics (red) from the predominantly normal faulting moment tensor. The synthetic fits the early Rayleigh pulse and the downward acoustic pulse but does not fit the late peak at 25 seconds.

We prefer to use the amplitude ratio between the acoustic and Rayleigh pulses rather than the absolute amplitude as the ratio is less sensitive to simulation uncertainties. The amplitude ratio is highly dependent to the source depth. For a shallow source, the acoustic pulse is amplified compared to the Rayleigh pulse (Figure S9), which is consistent with the infrasound observations for underground nuclear explosions (Averbuch, 2020). For source depths shallower than 1 km, the amplitude ratio is large due to stronger Rayleigh pulse; for deeper source depths, the amplitudes for both pulses are similarly weak. Other factors such as a slow layer near the surface do not affect deeper sources and can further increase the amplitude ratio for shallow sources. Based on qualitative comparison with the observed amplitude ratio, we estimate that the seismic source of the collapse events should be at depths shallower than 1 km. As a seismic magnitude of Mw 5.0 has a rupture length close to 1 km (Kanamori and Anderson, 1975), it is possible that the fault ruptured all the way to the surface, hence the seismic source depth is fixed at 450 m in the previous moment tensor analysis (Section 3.3).

The infrasound data has a late strong peak arriving at 25 seconds which is stronger in absolute amplitude than the initial downward pulse (Figure 7). The normal faulting solution, however, cannot fully fit the observed signal and only produces synthetics with peak equal or weaker amplitude than the downward pulse, regardless the source depths and near-surface source model. This mismatch in amplitude may potentially be accounted for by isotropic sources at 1 – 1.5 km depth, which has a weak peak arriving at the right time range, and points to a potential dual process of normal-faulting and inflation during the collapse event. While the topography is not expected to play a significant role for low-frequency acoustic waves, a detailed analysis which considers other important factors such as the interplay between the choice of source time function and velocity model is needed to accurately reproduce the absolute amplitude and is beyond the scope of this study.

## 5 Discussion

### 5.1 Factors controlling isotropic component

Seismic moment-tensor characterization is key to identify the source mechanism during volcanic eruptions (e.g., Bárðarbunga, Iceland (Gudmundsson et al., 2016; Ágústsdóttir et al., 2019), Piton de la Fournaise, Réunion Island (Duputel and Rivera, 2019; Fontaine et al., 2019), Miyake-jima, offshore Japan (Kumagai et al., 2001), and Kilauea, Hawaii (Alvizuri et al., 2021; this study). However, there are several factors that can affect the moment tensor, in particular the resolved isotropic component. In this study, we emphasized on the necessity of using near-field data to constrain the isotropic component and using other independent observational data to constrain depth. In Figure S10, we found that without the near-field data, the full moment tensor solutions for explosive and collapse events have negative isotropic component across all depths, indicating implosion which is inconsistent with the inflationary signal observed in tilt and GPS (Anderson et al., 2019). The results of negative isotropic component hold regardless of the choice of velocity models. There is also a strong correlation between depth and the strength of the isotropic component. Seismic moment tensor inversions alone have limited sensitivity for depth as they give similar error misfits for a range of depth with the smallest misfit at deeper depths. Therefore, other independent data, such as particle motion and infrasound, are important to constrain depth and, in turn, the isotropic component.

### 5.2 Asymmetric slip resolved from teleseismic moment tensor inversion

The 2018 Kilauea caldera collapse bears much resemblance to the 2014 Bárðarbunga caldera collapse in Iceland where the seismicity focused on one corner of the caldera and at shallow depths not deeper than 4 km (Ágústsdóttir et al., 2019). The source mechanisms at Bárðarbunga were also predominantly double-couple on inward-dipping normal faults. This asymmetric slip differs from the commonly assumed piston-type collapse where the entire ring fault slips during the caldera collapse. To confirm the partial ring-fault slip, we conducted another independent moment tensor inversion for all 50 collapse events using very long period teleseismic waves (over ~100 s). An advantage in using very-long period data is that complex velocity structures around the caldera will not affect the inversion results.

Because the small contribution to very long period seismic waves by the dip-slip components in shallow sources, there are large uncertainties in estimating the dip angle and seismic moment (Sandanbata et al., 2021). Hence, following the method in Sandanbata et al. (2021), we constrained the ring fault geometry by focusing only on the resolvable components of the inverted moment tensor: vertical CLVD ($M_{vCLVD}$) and strike-slip ($M_{SS}$) components (Text S1; Figure S11). This resolvable moment tensor ($M_{RES} = M_{vCLVD} + M_{SS}$) relates to the ring-fault geometry in two ways. Firstly, the ratio of CLVD moment to the resolvable moment ($k_{CLVD}$) positively correlates the short arc angle or the fraction of the ring fault that slipped (Figure S11c). Secondly, the direction of the pressure (P) axes of $M_{SS}$ gives the orientation of the fault plane measured at the midpoint of the curved fault (Figure S11d). The P-axis orientation and the relationship between $k_{CLVD}$ and the arc angle are independent of dip angle and scalar seismic moment and hence can be estimated without the dip-slip component. The procedure for the inversion is in Text S2. Note that there is a trade-off between vertical-P CLVD and pure positive isotropic sources due to the similarity in far-field waveforms (Figure S11) but we found that estimation of $k_{CLVD}$ is only reduced even when we assume an additional pure positive isotropic component for the inversion (see Text S2). Hence, we constrained zero isotropic contribution for the inversion to estimate the upper limit of the $k_{CLVD}$ value, enabling us to infer the maximum arc angle of the ring fault that slipped.

The results from the moment tensor inversion using global stations for all the 50 collapse events show normal-faulting focal mechanism with consistent $k_{CLVD}$ value and P-axis orientation (Figures S13 and S14). The $k_{CLVD}$ value is small, indicating the ring fault has partially slipped with an arc angle less than 90$^{o}$. The P-axis has a strike of northeast-southwest, which suggests the fault plane can be either along northwest or southeast corner of the ring fault. The teleseismic moment tensor solution is consistent with the inward-dipping normal faulting solution derived using regional stations and supports an asymmetric slip during the collapse events. The evolution in focal-mechanism properties throughout the collapse events, as seen in the local moment tensor inversion, cannot be observed at very-long periods.

### 5.3 Reconciling seismic, infrasound and geodetic observations

The characterization of the large seismic events at the Kilauea summit sheds light on the underlying mechanisms driving the complex sequence of early VLP-dominant events and subsequent broad-scale collapse events. There are several proposed mechanisms to explain the VLP signals at the Kilauea summit, including (1) gas slug ascending, expanding and eventual bursting, exciting the VLP signal at depth (Chouet et al., 2010), and (2) rockfalls impacting the lava lake, triggering both plume and VLP signal from the pressure transient transmitted along the conduit (Orr et al., 2013). During the 2018 eruption, the VLP seismic signal and plume generation were not necessarily linked, as degassing activity and plumes were still occasionally observed after the early VLP-dominant events have ceased. However, the consistency of the seismic source at the Halema'uma'u reservoir depth, obtained through particle motion studies, seismic moment tensor inversion, and infrasound analysis, suggests that the magma reservoir governs the seismic behavior. One way to generate an isotropic seismic signal is by pressurizing the magma chamber through an intrusion of an overburden roof or 'piston', resulting in transient expansion in reservoir, similar to the mechanism suggested for Miyake-jima volcano (Kumagai et al., 2001) and for Kilauea from geodetic observations (Segall et al., 2019, 2020). As the conduit empties during the eruption, rockfall could also be a possible trigger, generating explosions and degassing signals almost simultaneously. However, the later collapses show strong evidence for fault slipping, hence we suggest that the seismic events are a result of fault slipping into the Halema'uma'u reservoir, driven by magma withdrawal from summit.

Our finding is consistent with the geodetically-inferred 'slip and inflation' model by Segall et al. (2019 and 2020) where during the caldera collapse, the roof block slips into the Halema'uma'u reservoir, inducing a proportionate inflation within the reservoir. In particular, the GPS displacement pattern imposes that the slip should occur along a steep inward-dipping normal fault, which is consistent with our resolved focal mechanisms of shear slip along inward-dipping normal fault with an average dip of 75°. Unlike a symmetric ring-fault slip proposed by Segall et al. (2019 and 2020), two independent moment-tensor inversions show that the later collapses slip partially along the northwest corner of the caldera. The partial faulting may explain the asymmetry observed in GPS displacement where the geodetic model under-predicts the displacements along the northwest and southeast corners; and over-predicts those on the orthogonal corners.

With the constraints from near-field stations, particle motion and infrasound, we could conclude that an extended inflation occurred at the Halema'uma'u reservoir during the earlier events, as suggested by the long seismic source duration (10-20 seconds). There is also evidence for the 'slip' process expected from the inflation as all the early events show substantial (25%) double-couple contribution with strike, rake and dip values consistent to a normal faulting behavior. Based on the InSAR data, the slip may occur on a buried fault and only cause a minor surface depression close to the predicted center of the Halema'uma'u reservoir (Anderson et al., 2019).

For the later collapses, seismic data can detect the slip process but not the corresponding inflation which is inferred from the infrasound-simulation results. However, we postulate that the slip process happens before the inflation, which is consistent with the process described in 'slip and inflation' model (Segall et al., 2019 and 2020). Butler (2018) compiled stacked antipodal PKIKP polarities for the collapse events that capture the initial seismic energy propagating vertically downward away from the collapse source to the antipodal ends in southern Africa. These PKIKP phases show dilatational first motions which only fit solutions with minimal isotropic component at less than 5% (Figure S15), supporting an initial slip process.

### 5.4 Chronology of the Kilauea summit deformation

The chronology of the summit deformation during the 2018 eruption is summarized in Figure 8. The drop of lava lake elevation beginning May 2 indicates a reduction in the magma reservoir pressure (Anderson et al., 2019), causing the inert fault structures within the caldera, which was previously supported by the reservoir pressure, to fail. The slip intruded into the Halema'uma'u chamber, pressurized the chamber at depth, and generated long-duration isotropic signals. The slip also triggered a degassing process at depth where gas bubbles broke through the lava surface and ascended along the conduit as an ash-rich plume, which is consistent with the observed spikes in sulfur dioxide emission during the early inflationary events (Neal et al., 2019).

The transition from the early inflationary events to the later collapse events is intriguing as it coincides with a coalescence of fissure eruptions at the Lower East Rift Zone to a single fissure (Fissure 8) with high effusion rate (Neal et al., 2019). This high effusion rate may have accelerated the decrease of magma pressure at the summit, driving a series of normal-faulting collapse events. The initial collapses (May 29- June 7) have a relatively high CLVD component (~12%), which is an apparent effect of slip along curved faults. The later collapses (June 8 – 24, June 25 – August 2) have little CLVD component, indicating the faults are more linear. The rake also becomes increasingly negative and stays constant from June 25 onwards, suggesting the faulting behavior is becoming purely normal. Based on the increasing strike value and the eastward source migration observed in particle motion, the slips developed over time across continuous fault-like structures bounding the caldera. This fault could be the reactivation of a pre-existing ring-fault, the development of a new ring-fault structure or failures along pre-existing dike structures.

The most notable characteristics is that the caldera collapse is asymmetric, confined to the northwest corner of the caldera. There are a few potential scenarios that may have encouraged such asymmetry. Prior to 2018, Kilauea summit has experienced multiple episodes of fissure eruption, most recently in 1974 on the floor of Halema'uma'u crater (Holcomb, 1987) with similar strikes to the ones obtained in this study. The repeating eruption may have created heterogenous mechanical properties across the caldera, which fails under different stress thresholds, and contribute to the observed asymmetric collapse. The asymmetry can also be formed as the summit is subjected to a prevalent extensional stress due to a seaward motion of the volcano's south flank (Poland et al., 2014), which is reflected in the similar orientation of the pressure and tension axes observed in all the seismic events. The asymmetry does not preclude an overall subsidence of the roof block as a limited number of GPS stations within the caldera measured downward vertical displacement during the collapse (Neal et al., 2019), but indicates there is a more substantial slip on the northwest side.

The majority of the relocated large collapse events in Shelly and Thelen (2019) occurred at the northwest corner of the caldera, consistent with our findings (Figure S16). Shelly and Thelen (2019) also relocated the microseismicity clusters in between the caldera collapses and interestingly, they show a strong asymmetry, concentrating at the eastern half of the caldera opposite of the collapse fault plane. The occurrence frequency of the microseismicity has a consistent pattern of increasing from few and peaking right before the collapse event. The final topography images show an overall subsidence of the roof block by the end of the eruption (Lundgren et al., 2019), which may give the impression that the roof block dropped in a single block during each collapse. However, given the distribution of large slip and microseismicity, it is possible that the roof piston may have failed in a 'see-saw' manner in two stages: small continuous slips in the form of microseismicity on the southeast corner of the caldera, compensated by major large slips on the northwest corner during the large seismic events.

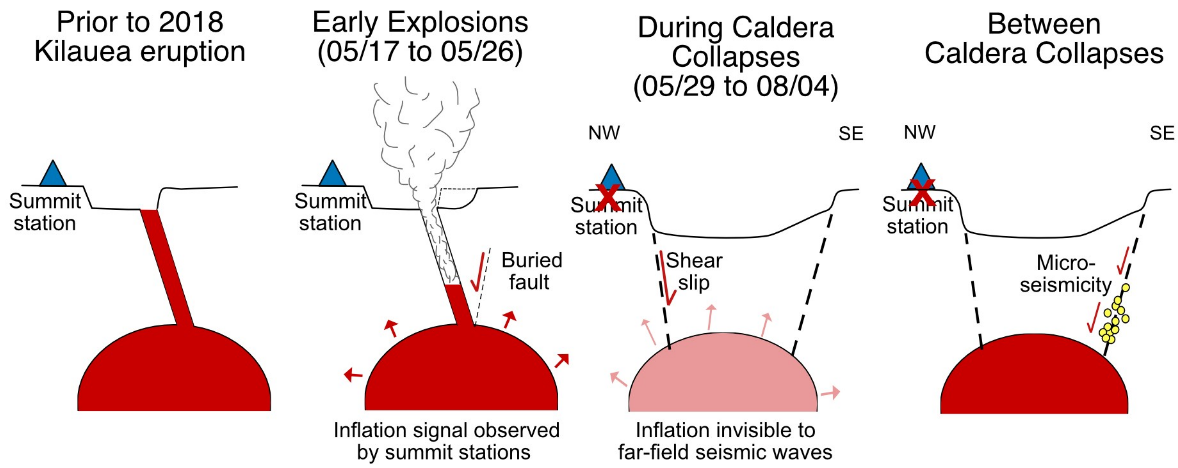


**Figure 8.** Schematic shows the chronology of the Kilauea summit deformation during the 2018 Kilauea eruption: **(1)** Prior to the eruption, the lava-lake level reached the vent and started to decrease on May 2. **(2)** The early seismic events show strong inflation signal observed by summit stations and are accompanied by occasional plume eruptions. Shear slip occurring on buried fault may cause a minor surface depression. **(3)** The asymmetric collapses are characterized as normal faulting along inward dipping fault on the northwest corner of the caldera. Inflations cannot be resolved without the summit stations. **(4)** In between the large collapses, microseismicity cluster are observed mostly at the southeast corner of the caldera.

## 6 Conclusions

Seismic and infrasound data reveal a complex deformation process at the Kilauea summit during the large seismic events, involving both inflation of the Halema'uma'u reservoir and a dominant asymmetric slip along the northwest corner of the caldera. Near-field summit stations were crucial to resolve the isotropic contribution in the early explosive events. Although the inflation for the later collapses cannot be resolved, the fault geometry for the later collapses, i.e., slip along inward-dipping normal fault, were determined using two independent moment tensor inversions. Infrasound data and particle motion analysis provide further constraints on source migration pattern, source location and length of the lava lake conduit above the Halema'uma'u reservoir. The asymmetric collapse at Kilauea can explain other features including microseismicity distribution and overestimation in geodetic modeling.

## Acknowledgments and Data

We are deeply grateful for Luis Rivera for his insights and help on the teleseismic moment tensor inversion, Greg Waite for providing the initial NPT infrasound data, and USGS – Hawaiian Volcano Observatory for their dedication in maintaining the geophysical monitoring network throughout the eruption. O.S. received funding from JSPS-KAKENHI (grant number: JP20J01689). All seismic and infrasound data used in this study are available through the IRIS webservices. The moment tensor catalogs are provided with details in the Supporting Information.

**References**

Ágústsdóttir, T., Winder, T., Woods, J., White, R. S., Greenfield, T., & Brandsdóttir, B. (2019). Intense Seismicity During the 2014–2015 Bárðarbunga-Holuhraun Rifting Event, Iceland, Reveals the Nature of Dike-Induced Earthquakes and Caldera Collapse Mechanisms. *Journal of Geophysical Research: Solid Earth*, *124*(8), 8331–8357. https://doi.org/10.1029/2018JB016010

Alvizuri, C. R., Matoza, R. S., & Okubo, P. G. (2021). Earthquake collapse mechanisms and periodic, migrating seismicity during the 2018 summit collapse at Kīlauea caldera. Earth and Planetary Science Letters, 562, 116819.

Anderson, K. R., Poland, M. P., Johnson, J. H., & Miklius, A. (2015). Episodic Deflation-Inflation Events at Kīlauea Volcano and Implications for the Shallow Magma System. In R. Carey, V. Cayol, M. Poland, & D. Weis (Eds.), *Geophysical Monograph Series* (pp. 229–250). John Wiley & Sons, Inc. https://doi.org/10.1002/9781118872079.ch11

Anderson, K. R., Johanson, I. A., Patrick, M. R., Gu, M., Segall, P., Poland, M. P., Montgomery-Brown, E. K., & Miklius, A. (2019). Magma reservoir failure and the onset of caldera collapse at Kīlauea Volcano in 2018. *Science*, *366*(6470), eaaz1822. https://doi.org/10.1126/science.aaz1822

Averbuch, G., Assink, J. D., & Evers, L. G. (2020). Long-range atmospheric infrasound propagation from subsurface sources. *The Journal of the Acoustical Society of America*, *147*(2), 1264-1274.

Baker, S., & Amelung, F. (2012). Top-down inflation and deflation at the summit of Kīlauea Volcano, Hawai'i observed with InSAR. *Journal of Geophysical Research: Solid Earth*, *117*, B12406. https://doi.org/10.1029/2011JB009123

Brissaud, Q., Martin, R., Garcia, R. F., & Komatitsch, D. (2017). Hybrid Galerkin numerical modelling of elastodynamics and compressible Navier–Stokes couplings: Applications to seismo-gravito acoustic waves. *Geophysical Journal International*, *210*(2), 1047–1069. https://doi.org/10.1093/gji/ggx185

Butler, R. (2019). Composite Earthquake Source Mechanism for 2018 Mw 5.2–5.4 Swarm at Kīlauea Caldera: Antipodal Source Constraint. *Seismological Research Letters*. https://doi.org/10.1785/0220180288

Chapman, C. H., & Leaney, W. S. (2012). A new moment-tensor decomposition for seismic events in anisotropic media: Moment-tensor decomposition. *Geophysical Journal International*, *188*(1), 343–370. https://doi.org/10.1111/j.1365-246X.2011.05265.x

Chouet, B. A., Dawson, P. B., James, M. R., & Lane, S. J. (2010). Seismic source mechanism of degassing bursts at Kilauea Volcano, Hawaii: Results from waveform inversion in the 10–50 s band. *Journal of Geophysical Research*, *115*(B9). https://doi.org/10.1029/2009JB006661

Contreras-Arratia, R., & Neuberg, J. W. (2020). Towards reconciling seismic and geodetic moment estimations: Case Bárðarbunga. *Journal of Volcanology and Geothermal Research*, *408*, 107034.

Dawson, P. B., Benítez, M. C., Chouet, B. A., Wilson, D., & Okubo, P. G. (2010). Monitoring very-long-period seismicity at Kilauea Volcano, Hawaii. *Geophysical Research Letters*, *37*(18). https://doi.org/10.1029/2010GL044418

Duputel, Z., & Rivera, L. (2019). The 2007 caldera collapse of Piton de la Fournaise volcano: Source process from very-long-period seismic signals. *Earth and Planetary Science Letters*, *527*, 115786. https://doi.org/10.1016/j.epsl.2019.115786

Fee, D., Garcés, M., Patrick, M., Chouet, B., Dawson, P., & Swanson, D. (2010). Infrasonic harmonic tremor and degassing bursts from Halema'uma'u Crater, Kilauea Volcano, Hawaii. *Journal of Geophysical Research*, *115*(B11). https://doi.org/10.1029/2010JB007642

Fee, D., & Matoza, R. S. (2013). An overview of volcano infrasound: From hawaiian to plinian, local to global. *Journal of Volcanology and Geothermal Research*, *249*, 123–139. https://doi.org/10.1016/j.jvolgeores.2012.09.002

Fontaine, F. R., Roult, G., Hejrani, B., Michon, L., Ferrazzini, V., Barruol, G., Tkalčić, H., Muro, A. D., Peltier, A., Reymond, D., Staudacher, T., & Massin, F. (2019). Very- and ultra-long-period seismic signals prior to and during caldera formation on La Réunion Island. *Scientific Reports*, *9*(1), 1–15. https://doi.org/10.1038/s41598-019-44439-1

Fukao, Y., Sandanbata, O., Sugioka, H., Ito, A., Shiobara, H., Watada, S., & Satake, K. (2018). Mechanism of the 2015 volcanic tsunami earthquake near Torishima, Japan. *Science Advances*, *4*(4), eaao0219. https://doi.org/10.1126/sciadv.aao0219

Gudmundsson, M. T., Jónsdóttir, K., Hooper, A., Holohan, E. P., Halldórsson, S. A., Ófeigsson, B. G., Cesca, S., Vogfjörd, K. S., Sigmundsson, F., Högnadóttir, T., Einarsson, P., Sigmarsson, O., Jarosch, A. H., Jónasson, K., Magnússon, E., Hreinsdóttir, S., Bagnardi, M., Parks, M. M., Hjörleifsdóttir, V., … Aiuppa, A. (2016). Gradual caldera collapse at Bárdarbunga volcano, Iceland, regulated by lateral magma outflow. *Science*, *353*(6296), aaf8988. https://doi.org/10.1126/science.aaf8988

Hejrani, B., & Tkalčić, H. (2020). Resolvability of the centroid−moment−tensors for shallow seismic sources and improvements from modelling high−frequency waveforms. *Journal of Geophysical Research: Solid Earth*, (February 2019), 1–13. https://doi.org/10.1029/2020JB019643

Holcomb, R. T. (1987). Eruptive history and long-term behavior of Kilauea Volcano. *US Geol. Surv. Prof. Pap*, 1350(1):261–350.

Julian, B. R., Miller, A. D., & Foulger, G. R. (1998). Non-double-couple earthquakes 1. Theory. *Reviews of Geophysics*, *36*(4), 525–549. https://doi.org/10.1029/98RG00716

Kanamori, H., & Anderson, D. L. (1975). Theoretical basis of some empirical relations in seismology. *Bulletin of the Seismological Society of America*, *65*(5), 1073–1095.

Kanamori, H., & Brodsky, E. E. (2004). The physics of earthquakes. *Reports on Progress in Physics*, *67*(8), 1429.

Kawakatsu, H. (1996). Observability of the isotropic component of a moment tensor. *Geophysical Journal International*, *126*(2), 525–544. https://doi.org/10.1111/j.1365-246X.1996.tb05308.x

Kawakatsu, H., Kaneshima, S., Matsubayashi, H., Ohminato, T., Sudo, Y., Tsutsui, T., Uhira, K., Yamasato, H., Ito, H., & Legrand, D. (2000). Aso94: Aso seismic observation with broadband instruments. *Journal of Volcanology and Geothermal Research*, *101*(1–2), 129–154. https://doi.org/10.1016/S0377-0273(00)00166-9

Kobayashi, T., Ida, Y., & Ohminato, T. (2005). Small inflation sources producing seismic and infrasonic pulses during the 2000 eruptions of Miyake-jima, Japan. *Earth and Planetary Science Letters*, *240*(2), 291–301. https://doi.org/10.1016/j.epsl.2005.09.015

Kumagai, H. Ohminato, T., Nakano, M., Ooi, M., Kubo, A., Inoue, H., & Oikawa, J. (2001). Very-Long-Period Seismic Signals and Caldera Formation at Miyake Island, Japan. *Science*, *293*(5530), 687–690. https://doi.org/10.1126/science.1062136

Liang, C., Crozier, J., Karlstrom, L., & Dunham, E. M. (2020). Magma Oscillations in a Conduit-Reservoir System, Application to Very Long Period (VLP) Seismicity at Basaltic Volcanoes: 2. Data Inversion and Interpretation at Kīlauea Volcano. *Journal of Geophysical Research: Solid Earth*, *125*(1), e2019JB017456. https://doi.org/10.1029/2019JB017456

Liang, C., & Dunham, E. M. (2020). Lava lake sloshing modes during the 2018 Kīlauea Volcano eruption probe magma reservoir storativity. *Earth and Planetary Science Letters*, *535*, 116110. https://doi.org/10.1016/j.epsl.2020.116110

Lin, G., Shearer, P. M., Matoza, R. S., Okubo, P. G., & Amelung, F. (2014). Three-dimensional seismic velocity structure of Mauna Loa and Kilauea volcanoes in Hawaii from local seismic tomography. *Journal of Geophysical Research: Solid Earth*, *119*(5), 4377–4392. https://doi.org/10.1002/2013JB010820

Lundgren, P. R., Bagnardi, M., & Dietterich, H. (2019). Topographic Changes During the 2018 Kīlauea Eruption from Single−pass Airborne InSAR. *Geophysical Research Letters*. https://doi.org/10.1029/2019GL083501

Orr, T. R., Thelen, W. A., Patrick, M. R., Swanson, D. A., & Wilson, D. C. (2013). Explosive eruptions triggered by rockfalls at Kīlauea volcano, Hawaiʻi. *Geology*, *41*(2), 207–210. https://doi.org/10.1130/G33564.1

Patrick, M. R., Harris, A. J. L., Ripepe, M., Dehn, J., Rothery, D. A., & Calvari, S. (2007). Strombolian explosive styles and source conditions: Insights from thermal (FLIR) video. *Bulletin of Volcanology*, *69*(7), 769–784. https://doi.org/10.1007/s00445-006-0107-0

Patrick, M. R., Anderson, K. R., Poland, M. P., Orr, T. R., & Swanson, D. A. (2015). Lava lake level as a gauge of magma reservoir pressure and eruptive hazard. *Geology*, *43*(9), 831–834. https://doi.org/10.1130/G36896.1

Patrick, M. R., Dietterich, H. R., Lyons, J. J., Diefenbach, A. K., Parcheta, C., Anderson, K. R., Namiki, A., Sumita, I., Shiro, B., & Kauahikaua, J. P. (2019). Cyclic lava effusion during the 2018 eruption of Kīlauea Volcano. *Science*, *366*(6470). https://doi.org/10.1126/science.aay9070

Poland, M. P., Miklius, A., & Montgomery-Brown, E. K. (2014). Magma supply, storage, and transport at shield-stage Hawaiian volcanoes. In *Magma supply, storage, and transport at shield-stage Hawaiian volcanoes* (USGS Numbered Series No. 1801–5; Professional Paper, Vols. 1801–5, p. 56). U.S. Geological Survey. https://doi.org/10.3133/pp18015

Neal, C. A., Brantley, S. R., Antolik, L., Babb, J. L., Burgess, M., Calles, K., Cappos, M., Chang, J. C., Conway, S., Desmither, L., Dotray, P., Elias, T., Fukunaga, P., Fuke, S., Johanson, I. A., Kamibayashi, K., Kauahikaua, J., Lee, R. L., Pekalib, S., … Damby, D. (2019). The 2018 rift eruption and summit collapse of Kīlauea Volcano. *Science*, *363*(6425), 367–374. https://doi.org/10.1126/science.aav7046

Sandanbata, O., Kanamori, H., Rivera, L., Zhan, Z., Watada, S., & Satake, K. (2021). Moment tensors of ring-faulting at active volcanoes: Insights into vertical-CLVD earthquakes at the Sierra Negra caldera, Galapagos Islands. *Earth and Space Science Open Archive; Earth and Space Science Open Archive*. https://doi.org/10.1002/essoar.10505947.1

Segall, P., Anderson, K. R., Johanson, I., & Miklius, A. (2019). Mechanics of Inflationary Deformation During Caldera Collapse: Evidence From the 2018 Kīlauea Eruption. *Geophysical Research Letters*, *46*(21), 11782–11789. https://doi.org/10.1029/2019GL084689

Segall, P., Anderson, K. R., Pulvirenti, F., Wang, T., & Johanson, I. (2020). Caldera Collapse Geometry Revealed by Near-Field GPS Displacements at Kīlauea Volcano in 2018. *Geophysical Research Letters*, *47*(15), e2020GL088867. https://doi.org/10.1029/2020GL088867

Shelly, D. R., & Thelen, W. A. (2019). Anatomy of a Caldera Collapse: Kīlauea 2018 Summit Seismicity Sequence in High Resolution. *Geophysical Research Letters*, *46*(24), 14395–14403. https://doi.org/10.1029/2019GL085636

Taddeucci, J., Scarlato, P., Capponi, A., Bello, E. D., Cimarelli, C., Palladino, D. M., & Kueppers, U. (2012). High-speed imaging of Strombolian explosions: The ejection velocity of pyroclasts. *Geophysical Research Letters*, *39*(2). https://doi.org/10.1029/2011GL050404

Tepp, G., Hotovec-Ellis, A., Shiro, B., Johanson, I., Thelen, W., & Haney, M. M. (2020). Seismic and geodetic progression of the 2018 summit caldera collapse of Kīlauea volcano. *Earth and Planetary Science Letters*, *540*, 116250. https://doi.org/10.1016/j.epsl.2020.116250

Wielandt, E., & Forbriger, T. (1999). Near-field seismic displacement and tilt associated with the explosive activity of Stromboli. *Annals of Geophysics*, *42*(3).

Zhao, L.-S., & Helmberger, D. V. (1994). Source estimation from broadband regional seismograms. *Bulletin of the Seismological Society of America*, *84*(1), 91–104.

Zhu, L., & Ben-Zion, Y. (2013). Parametrization of general seismic potency and moment tensors for source inversion of seismic waveform data. *Geophysical Journal International*, *194*(2), 839–843. https://doi.org/10.1093/gji/ggt137

Zhu, L., & Helmberger, D. V. (1996). Advancement in source estimation techniques using broadband regional seismograms. *Bulletin of the Seismological Society of America*, *86*(5), 1634–1641.

Zhu, L., & Rivera, L. A. (2002). A note on the dynamic and static displacements from a point source in multilayered media: A note on the dynamic and static displacements from a point source. *Geophysical Journal International*, *148*(3), 619–627. https://doi.org/10.1046/j.1365-246X.2002.01610.x

**References for supporting information**

Duputel, Z., Rivera, L., Kanamori, H., & Hayes, G. (2012). W phase source inversion for moderate to large earthquakes (1990–2010). *Geophysical Journal International*, *189*(2), 1125–1147. https://doi.org/10.1111/j.1365-246X.2012.05419.x

Hayes, G. P., Rivera, L., & Kanamori, H. (2009). Source Inversion of the W-Phase: Real-time Implementation and Extension to Low Magnitudes. *Seismological Research Letters*, *80*(5), 817–822. https://doi.org/10.1785/gssrl.80.5.817

Kanamori, H., & Rivera, L. (2008). Source inversion of W phase: Speeding up seismic tsunami warning. *Geophysical Journal International*, *175*(1), 222–238. https://doi.org/10.1111/j.1365-246X.2008.03887.x

Sandanbata, O., Kanamori, H., Rivera, L., Zhan, Z., Watada, S., & Satake, K. (2021). Moment tensors of ring-faulting at active volcanoes: Insights into vertical-CLVD earthquakes at the Sierra Negra caldera, Galapagos Islands. *Earth and Space Science Open Archive; Earth and Space Science Open Archive*. https://doi.org/10.1002/essoar.10505947.1